Biophysical Journal Volume 95 September 2008 2624–2635

Computational Modeling of Three-Dimensional Electrodiffusion in Biological Systems: Application to the Node of Ranvier

Courtney L. Lopreore,*† Thomas M. Bartol,†‡ Jay S. Coggan,*† Daniel X. Keller,†§‖
Gina E. Sosinsky,¶ Mark H. Ellisman,¶ and Terrence J. Sejnowski*†‡§
*Howard Hughes Medical Institute and †The Salk Institute for Biological Studies, La Jolla, California 92037; and ‡Center for Theoretical Biological Physics, §Division of Biological Sciences, ¶National Center for Microscopy and Imaging Research, Center for Research in Biological Systems, and Department of Neurosciences, and ‖Neurosciences Graduate Program, University of California, San Diego, La Jolla, California 92093

ABSTRACT A computational model is presented for the simulation of three-dimensional electrodiffusion of ions. Finite volume techniques were used to solve the Poisson-Nernst-Planck equation, and a dual Delaunay-Voronoi mesh was constructed to evaluate fluxes of ions, as well as resulting electric potentials. The algorithm has been validated and applied to a generalized node of Ranvier, where numerical results for computed action potentials agree well with cable model predictions for large clusters of voltage-gated ion channels. At smaller channel clusters, however, the three-dimensional electrodiffusion predictions diverge from the cable model predictions and show a broadening of the action potential, indicating a significant effect due to each channel's own local electric field. The node of Ranvier complex is an elaborate organization of membrane-bound aqueous compartments, and the model presented here represents what we believe is a significant first step in simulating electrophysiological events with combined realistic structural and physiological data.

INTRODUCTION

Ionic electrodiffusion is an important part of the process of electrical conduction in neuronal cells. Theoretical studies of action potential propagation have relied on one-dimensional cable theory (implemented in modeling environments such as NEURON and GENESIS (1–3)). In cable theory, ionic concentrations are fixed in space, and the equilibrium potential of each ion is represented by a constant battery, whose electromotive force is given by the Nernst potential (4,5). A resting membrane potential is maintained by ionic concentration differences across the membrane, but intra- and extracellular concentration ratios remain the same during activity (6). On large spatial scales, such as in the squid giant axon, the concentration gradients change slowly, so using constant batteries is a good approximation. On smaller scales, however, there can be significant concentration gradients within the nanodomains and small compartments surrounding the voltage-gated ion channels. The batteries in these regions, therefore, need to be variable and dynamic to accurately model the local environment.

Models based on the Nernst-Planck equation have been used to model voltage-dependent concentration gradients. In previous work, Qian and Sejnowski (7) applied the Nernst-Planck equation in one dimension to model excitatory postsynaptic potentials on dendritic spines, and showed that when there are large conductance changes, there are significant discrepancies between the cable and electrodiffusion models. In other work, van Egeraat and Wikswo (8) applied a one-dimensional Nernst-Planck formulation to study axonal propagation in injured axons over long time scales.

The node of Ranvier is an integral component in myelinated axons, and dysfunction of the nodal complex plays an important role in neurological disorders such as multiple sclerosis, Guillain-Barre syndrome, and Charcot-Marie-Tooth disease. The node of Ranvier has a unique and complex geometrical structure, made up of many specialized compartments in which the accumulation and depletion of ions due to spatial irregularities can be observed. In this study, we apply a three-dimensional (3D) electrodiffusion method to a generalized nodal model. For the purpose of validating the 3D electrodiffusion method, we used well-established data for channel kinetics, and a simplified geometry of this extremely complex object. The accumulation and depletion of ions surrounding the node of Ranvier, demonstrated by the model, shows that the approximation of electroneutrality is invalid for cases where the geometric structure is nonuniform in space.

THEORY AND MODELING DETAILS

Electrodiffusion model

The electrodiffusion model includes the Nernst-Planck equations (9), which describe how ionic fluxes at given locations depend on diffusion, ion concentration, as well as the electric field. The Nernst-Planck equation is

$$\vec{J}_{\mathrm{k}} = -D_{\mathrm{k}}(\vec{\nabla} c_{\mathrm{k}} + (c_{\mathrm{k}}/\alpha_{\mathrm{k}})\vec{\nabla} V), \tag{1}$$

where V is the potential due to the distribution of electric charge, $\vec{J}_{\mathrm{k}}$ is the flux of ionic species k (number of particles per unit area, per unit time), D_{k} is the diffusion constant, c_{k} is the concentration of ionic species k, and $\alpha_{\mathrm{k}} = RT/Fz_{\mathrm{k}}$, where z_{k} is the valence of ionic species k, R is the gas constant, F is

---

Submitted February 22, 2008, and accepted for publication May 15, 2008.

Address reprint requests to Terrence J. Sejnowski, The Salk Institute for Biological Studies, 10010 N. Torrey Pines Road, La Jolla, CA 92037. Tel.: 858-453-4100, ext. 1280; Fax: 858-587-0417; E-mail: terry@salk.edu.

Editor: Richard W Aldrich.

0006-3495/08/09/2624/12 $2.00

doi: 10.1529/biophysj.108.132167

the Faraday constant, and T is the absolute temperature. The ionic concentrations and currents must satisfy the continuity equation

$$\vec{\nabla}\cdot\vec{J}_{\mathrm{k}}+\frac{\partial c_{\mathrm{k}}}{\partial t}=0. \tag{2}$$

Substituting Eq. 1 into Eq. 2, we get

$$\frac{\partial c_{\mathrm{k}}}{\partial t}=\vec{\nabla}\cdot\left[D_{\mathrm{k}}\left(\vec{\nabla}c_{\mathrm{k}}+\left(\frac{c_{\mathrm{k}}}{\alpha_{\mathrm{k}}}\right)\vec{\nabla}V(\vec{r},t)\right)\right]. \tag{3}$$

The electric potential, which is a function of space and time, is determined by solving the Poisson equation

$$\vec{\nabla}\cdot[\varepsilon(\vec{r})\vec{\nabla}V(\vec{r},t)]=-\rho(\vec{r}), \tag{4}$$

where $\varepsilon(\vec{r})$ is the dielectric constant of the medium and $\rho(\vec{r})$ is the charge density at position $\vec{r}$,

$$\rho(\vec{r})=\sum_{\mathrm{k}}c_{\mathrm{k}}z_{\mathrm{k}}F. \tag{5}$$

Finite volume formulation

If we integrate Eq. 2 over a volume Ω, we get

$$\iiint_{\Omega}\left(\frac{\partial c_{\mathrm{k}}}{\partial t}+\vec{\nabla}\cdot\vec{J}_{\mathrm{k}}\right)d\Omega=0. \tag{6}$$

Using the divergence theorem, we get

$$\iiint_{\Omega}\frac{\partial}{\partial t}c_{\mathrm{k}}d\Omega+\oint\!\!\oint_{\mathrm{s}}(\vec{J}_{\mathrm{k}}\cdot\hat{n})dS=0, \tag{7}$$

where S is the surface that bounds the domain Ω and $\hat{n}$ is the outward unit vector normal to the surface.

To evaluate the electric potential in the finite-volume formulation, Eq. 4 is also integrated, giving

$$\iiint_{\Omega}\vec{\nabla}\cdot[\varepsilon(\vec{r})\vec{\nabla}V]d\Omega=-\iiint_{\Omega}\rho(\vec{r})d\Omega. \tag{8}$$

Using the divergence theorem, this equation becomes

$$\oint\!\!\oint_{\mathrm{s}}\hat{n}\cdot\varepsilon(\vec{r})\vec{\nabla}VdS=-\iiint_{\Omega}\rho(\vec{r})d\Omega. \tag{9}$$

In the numerical solution of the problem, Eqs. 7 and 9 are solved in each cell of an irregular grid covering the domain of interest. Fluxes from one cell to another couple the equations.

Mesh generation

Properties of Delaunay-Voronoi meshes

The geometric properties of Delaunay-Voronoi dual meshes are very well suited to the requirements of the finite volume method, especially in irregularly shaped computational domains with complex boundary conditions. To illustrate the desirable properties, let us first consider a simple two-dimensional (2D) computational domain as shown in Fig. 1. The 2D domain is composed of two regions separated by a boundary (*green line*) and is sampled by a set of points, some of which lie on the boundary. Discussion of the methods for choosing where to place these points is beyond the scope of this article and is a very active area of research in computational geometry. Any such set of points can be tessellated into a Voronoi mesh (Fig. 1 *E*) and its geometric dual, a Delaunay triangular mesh (Fig. 1 *C*). The 2D Voronoi mesh is composed of Voronoi cells, which are convex polygons. Each Voronoi cell corresponds to the region of space closer to a given sample point than to any other point. One such cell is highlighted in red in Fig. 1, *D* and *E*. In 2D, the Delaunay mesh is composed of triangles, which are formed by connecting the sample points in adjacent Voronoi cells with one another. The Delaunay triangles also have the property that the circle circumscribing the three points of a given triangle will not contain any other sample points in its interior (Fig. 1 *B*). The circumcenters of the Delaunay triangles coincide with the corners of the Voronoi cells. Thus, given a Voronoi mesh, one can derive the Delaunay mesh and vice versa.

Fig. 2 shows how the Delaunay-Voronoi mesh duality extends to 3D. In this case, we form Delaunay tetrahedra that are circumscribed by spheres whose centers are the corners of 3D Voronoi polyhedra. We can now articulate the useful properties of Delaunay-Voronoi meshes for finite volume methods in 3D:

1. The edges of the Delaunay tetrahedra are perpendicular to a bounding face of a Voronoi cell. Fluxes and forces act along these edges. The lengths of the Delaunay tetrahedra edges are denoted as ΔR and represent the distance between centers of contiguous Voronoi cells across a cell face.
2. The area of each bounding face of a Voronoi cell is denoted as ΔS.
3. The Voronoi cells completely tile space and the volume of each cell is denoted $\Delta\Omega$.

3D Delaunay-Voronoi mesh of node of Ranvier

The node of Ranvier is composed of three distinct regions: the intracellular axoplasm, the myelin, and the extracellular space. For simplicity, we chose to model the myelin (including the axonal membrane) as a single material with a uniform dielectric coefficient, rather than explicity model the actual helical structure. A canonical 3D Delaunay-Voronoi dual mesh of a node of Ranvier (cross section shown in Fig. 3) was constructed in three steps.

Step 1. NETGEN (http://www.hpfem.jku.at/netgen/) was used to create a high-quality surface mesh of a 4 μm length of simplified axon with myelin, nodal region, and extracellular space. The dimensions of the axon, myelin, and nodal region were derived from EM tomograms of mammalian myelinated peripheral nerve (10) (see Table 1.). The distance to the outer boundary of the extracellular space was chosen to be as small as possible (to minimize computational cost) while still ensuring that the imposed boundary condition at this boundary (i.e., clamped at 0 V) did not create a simulation artifact at the outer surface of the myelin and axon membrane (see Results below). The quality surface mesh was composed of 7,713 vertices and 15,414 nearly equilateral triangles.

Step 2. The quality surface mesh was used as input to TetGen (http://tetgen.berlios.de/) to generate a quality Delaunay tetrahedral mesh that conformed to the boundaries represented by the surface mesh. The Delaunay volume mesh was composed of 12,584 vertices and 72,105 tetrahedra.

Step 3. A multimaterial Voronoi mesh was derived from the Delaunay mesh using our own algorithm. As the domain is composed of three distinct material regions (extracellular, myelin, and axoplasm) there are Voronoi cells that are cut by the boundaries of the different regions, and care was taken in the numerical implementation to avoid ion diffusion across two interfaces. Since there are 12,584 vertices in the Delaunay mesh, the Voronoi mesh contains this same number of whole cells (i.e., before dividing cells along material interfaces).

Discrete form of the equations

Using discrete volume elements defined by the Voronoi cells, cell i is assumed to have volume $\Delta\Omega_{\mathrm{i}}$ and having N_{i} faces. The surface area of face j of cell i is denoted by ΔS_{ij}, the outward unit normal vector of that face by $\hat{n}_{\mathrm{ij}}$. Using the discrete form of the flux of species k across face j of cell i, Eq. 1 becomes

$$\hat{n}_{\mathrm{ij}}\cdot(\vec{J}_{\mathrm{k}})_{\mathrm{ij}}=-D_{\mathrm{k}}[\hat{n}_{\mathrm{ij}}\cdot\vec{\nabla}(c_{\mathrm{k}})_{\mathrm{ij}}+(c_{\mathrm{k}}/\alpha_{\mathrm{k}})(\hat{n}_{\mathrm{ij}}\cdot\vec{\nabla}V_{\mathrm{ij}})]. \tag{10}$$

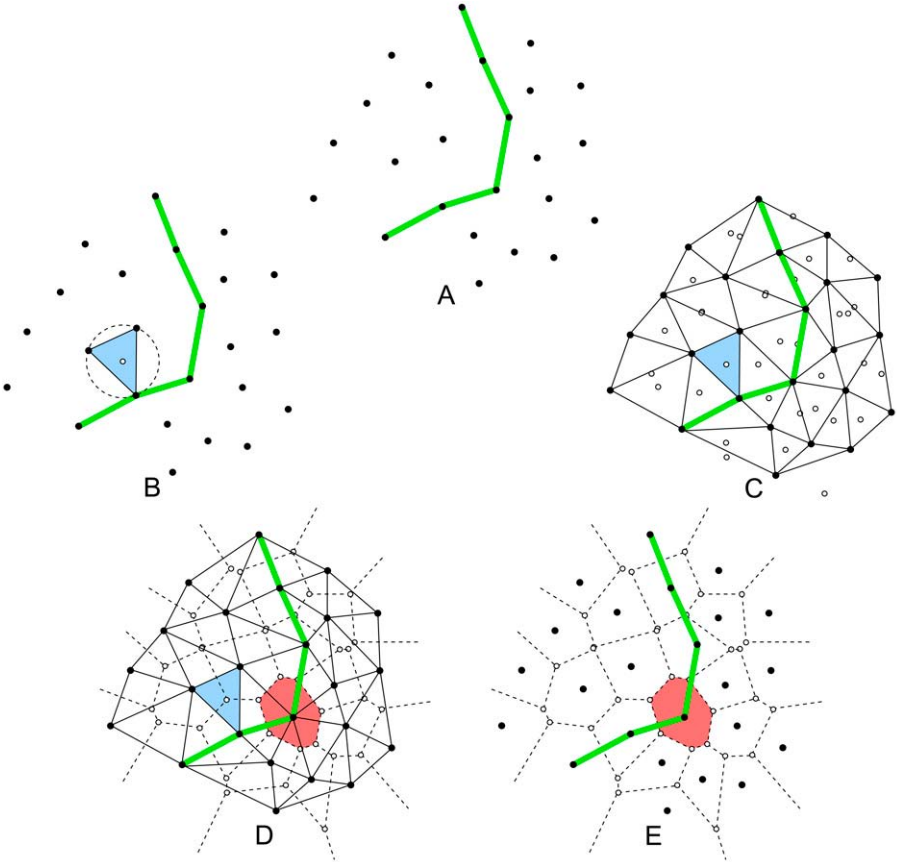

FIGURE 1 Relationships between Delaunay and Voronoi meshes in 2D. (*A*) Collection of points (*black dots*) sampling a 2D domain. Several of the points lie on a boundary (*green lines*) embedded in the domain. (*B*) A triangle (*blue*) formed from three points circumscribed by a circle that does not enclose any other points satisfies the Delaunay criterion. The center of the circumscribing circle is shown as a white dot. (*C* and *D*) 2D Delaunay mesh (*solid lines*) formed by Delaunay triangles. Triangle circumcenters are shown as white dots in *C* and *D*. (*D* & *E*). Voronoi cell (*red*) is formed by joining circumcenters of all triangles that share a common point. The collection of Voronoi cells comprises the Voronoi mesh (*dashed lines*). Note that the green boundary line cuts the red Voronoi cell into two regions.

Using a second-order differencing of the concentrations and electric potential, we get

$$\hat{n}_{\mathrm{ij}}\cdot\vec{\nabla}V_{\mathrm{ij}}\approx\frac{V_{\mathrm{j}}-V_{\mathrm{i}}}{\Delta R_{\mathrm{ij}}}\tag{11}$$

and

$$\hat{n}_{\mathrm{ij}}\cdot\vec{\nabla}(c_{\mathrm{k}})_{\mathrm{ij}}\approx\frac{(c_{\mathrm{k}})_{\mathrm{j}}-(c_{\mathrm{k}})_{\mathrm{i}}}{\Delta R_{\mathrm{ij}}}.\tag{12}$$

Now Eq. 7 is applied to the Voronoi cell *i* resulting in

$$\frac{\partial}{\partial t}(c_{\mathrm{k}})_{\mathrm{i}}\Delta\Omega_{\mathrm{i}}+\sum_{\mathrm{j=1}}^{N_{\mathrm{i}}}(\vec{J}_{\mathrm{k}})_{\mathrm{ij}}\cdot\hat{n}_{\mathrm{ij}}\Delta S_{\mathrm{ij}}=0.\tag{13}$$

In discrete form, Eq. 9 can be represented as

$$\sum_{\mathrm{j=1}}^{N_{\mathrm{i}}}\varepsilon_{\mathrm{ij}}\hat{n}_{\mathrm{ij}}\cdot\vec{\nabla}V_{\mathrm{ij}}\Delta S_{\mathrm{ij}}=-\rho_{\mathrm{i}}\Delta\Omega_{\mathrm{i}},\tag{14}$$

where $\varepsilon_{\mathrm{ij}}$ is the dielectric at face *j* of cell *i* and $\vec{\nabla}V_{\mathrm{ij}}$ is the voltage gradient at face *j*. Since the dielectric values are known at the cell nodes *i* and *j*, we can use an effective boundary permittivity $\varepsilon_{\mathrm{ij}}=2\varepsilon_{\mathrm{i}}\varepsilon_{\mathrm{j}}/(\varepsilon_{\mathrm{i}}+\varepsilon_{\mathrm{j}})$, the harmonic mean of the permittivity layers.

Using this approximation and Eq. 11, we finally arrive at the following form of Eq. 14:

$$-V_{\mathrm{i}}\left(\sum_{\mathrm{j=1}}^{N_{\mathrm{i}}}\varepsilon_{\mathrm{ij}}\frac{\Delta S_{\mathrm{ij}}}{\Delta R_{\mathrm{ij}}}\right)+\sum_{\mathrm{j=1}}^{N_{\mathrm{i}}}V_{\mathrm{j}}\varepsilon_{\mathrm{ij}}\frac{\Delta S_{\mathrm{ij}}}{\Delta R_{\mathrm{ij}}}=-\rho_{\mathrm{i}}\Delta\Omega_{\mathrm{i}}.\tag{15}$$

This equation is used to construct a system of linear algebraic equations for the unknown potentials V_{i} at the Voronoi cell centers. If there are a total N_{cells} of Voronoi cells, the system of equations in Eq. 15 is written in matrix form as

$$A\vec{v}=\vec{b},\tag{16}$$

where $\vec{v}=\langle V_1,V_2,\ldots,V_{\mathrm{Ncells}}\rangle$ and the vector $\vec{b}$ has elements $b_{\mathrm{i}}=-\rho_{\mathrm{i}}\Delta\Omega_{\mathrm{i}}$. Notice that the diagonal entries of matrix *A* are

$$A_{\mathrm{ii}}=-\sum_{\mathrm{j=1}}^{N_{\mathrm{i}}}\varepsilon_{\mathrm{ij}}\frac{\Delta S_{\mathrm{ij}}}{\Delta R_{\mathrm{ij}}}\tag{17}$$

and the off-diagonal entries are

$$A_{\mathrm{ij}}=\begin{cases}\varepsilon_{\mathrm{ij}}\dfrac{\Delta S_{\mathrm{ij}}}{\Delta R_{\mathrm{ij}}} & \text{if}\quad j\text{ is a neighbor of }i\text{ and }j\neq i\\ 0 & \text{if}\quad j\text{ is not a neighbor of }i\end{cases}.\tag{18}$$

Note that since this is an irregular grid, different cells may have a different number of neighbors; the number of neighbors of cell *i* gives the number of nonzero entries in the *i*th row of the matrix. In a regular Cartesian grid, each cell has four neighbors and the matrix would have five nonzero diagonals. Also note that the sum of all the elements of row *i* is

$$\sum_{\mathrm{j=1}}^{N_{\mathrm{cells}}}A_{\mathrm{ij}}=A_{\mathrm{ii}}+\sum_{\mathrm{j=1}}^{N_{\mathrm{i}}}\varepsilon_{\mathrm{ij}}\frac{\Delta S_{\mathrm{ij}}}{\Delta R_{\mathrm{ij}}}=0\tag{19}$$

(since the last sum is over the neighbors of cell *i*). This equation reflects the fact that the total flux into a cell is the sum of the fluxes from its abutting neighbors.

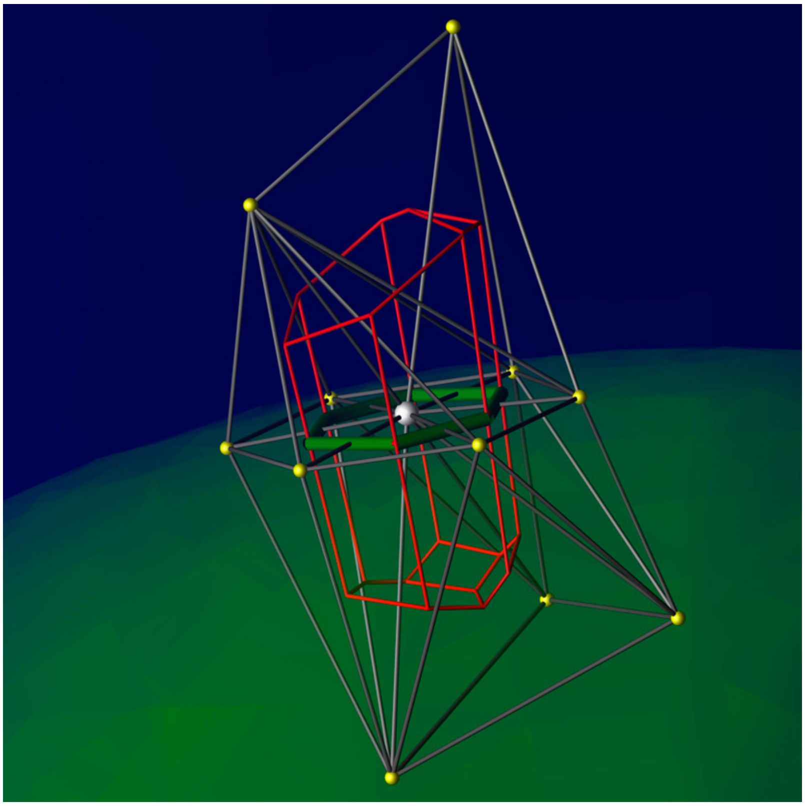

FIGURE 2 Relationships between Delaunay and Voronoi meshes in 3D. Enlarged view of Delaunay tetrahedra (*dark gray*) and a multimaterial Voronoi volume element (*red*) at the interface between the membrane (*green*) and extracellular space (*blue*) (see Fig. 3.). A single mesh vertex lying on the membrane interface is shown as a small white sphere. The Voronoi volume element associated with this vertex is shown as a red wire-frame polyhedron. Delaunay tetrahedra that share the white vertex are shown as dark gray wire frames with yellow vertices. The yellow vertices and white vertex are analogous to the black points in Fig. 1. The white vertex is also analogous to a black dot lying on the green boundary line shown in Fig. 1. The corners of the red Voronoi polyhedron are analogous to the white dots in Fig. 1. The surface element that lies at the membrane interface is shown as a green wire-frame polygon and is analogous to a portion of the green line shown in Fig. 1. Note that this surface element cuts the Voronoi element into two pieces—one that lies entirely in the blue extracellular space, and one that lies entirely in the green membrane.

Electrodiffusion model boundary conditions

A Dirichlet condition is imposed on the outermost boundary, Γ_b, the boundary of the extracellular space,

$$c_k(\vec{R}_b;t) = c_{o_k}, \quad \text{for} \quad \vec{R}_b \in \Gamma_b, \tag{20}$$

where c_o denotes the outer concentration of ionic species k. Similarly, the voltage obeys

$$V(\vec{R}_b,t) = 0, \quad \text{for} \quad \vec{R}_b \in \Gamma_b. \tag{21}$$

The fixed concentrations and a grounded voltage on the outermost boundary provide an infinite source/sink of ions during the simulation. Since there must be no flux of ions into or out of the membrane lacking channels, a Neumann boundary condition is imposed on the membrane Γ_a,

$$\hat{n} \cdot \nabla c_k = 0 \text{ on } \Gamma_a \text{ for all species } k. \tag{22}$$

The voltage is continuous across the membrane Γ_a.

Kinetic model for action potentials

Channels using Hodgkin-Huxley kinetics have discrete-state counterparts (6,12,13). We used stochastic models with transitions governed by the α- and β-rates, shown in Fig. 4. The equations governing transition from closed to open states are given by

$$\alpha_m(\mathrm{Na}) = 0.1\frac{\mathrm{V}+40}{1-e^{-0.1(\mathrm{V}+40)}} \tag{23}$$

$$\beta_m(\mathrm{Na}) = 4e^{-\frac{\mathrm{V}+65}{18}} \tag{24}$$

$$\alpha_h(\mathrm{Na}) = 0.07e^{-0.05(\mathrm{V}+65)} \tag{25}$$

$$\beta_h(\mathrm{Na}) = \frac{1}{1+e^{-0.1(\mathrm{V}+35)}} \tag{26}$$

$$\alpha_n(\mathrm{K}) = 0.01\frac{\mathrm{V}+55}{1-e^{-0.1(\mathrm{V}+55)}} \tag{27}$$

$$\beta_n(\mathrm{K}) = 0.125e^{-\frac{\mathrm{V}+65}{80}}, \tag{28}$$

where V is the voltage.

Description of cable model

Before applying the electrodiffusion method to a three-dimensional system, a one-dimensional model of a myelinated axonal node region was constructed using the NEURON Simulator (1,2). A three-compartment model was assembled with a single nodal segment (0.7 μm long, 0.868 μm diameter) flanked by two myelin segments (each 1.65 μm long, 0.868 μm diameter). Hodgkin-Huxley style Na^+ and K^+ channels were located in the node compartment only. Corresponding passive and active membrane properties, channel densities, and ion concentrations are listed in Table 2. All three compartments were assigned a 2 μm-high Frankenhaeuser space (FS) (14) that contained the extracellular ionic dynamics from which concentrations over time were calculated. Beyond the FS, the external world Na^+ and K^+ concentrations were clamped at initial values (Table 2). The equilibrium between the FS and external world were governed by a variable rate constant. Intracellular spaces were divided into four concentric rings (cylinders) that permitted lateral, cross-compartmental movement of Na^+ and K^+. In the cable model, boundary conditions at the myelin segment ends were reflective. A membrane action potential was evoked by injection of a square current pulse (10 pA, 0.5 ms) at the center of the node segment. A schematic diagram of the model is depicted in Fig. 5. The cable model was used to validate the electrodiffusion method by using the same kinetic and stimulus parameters.

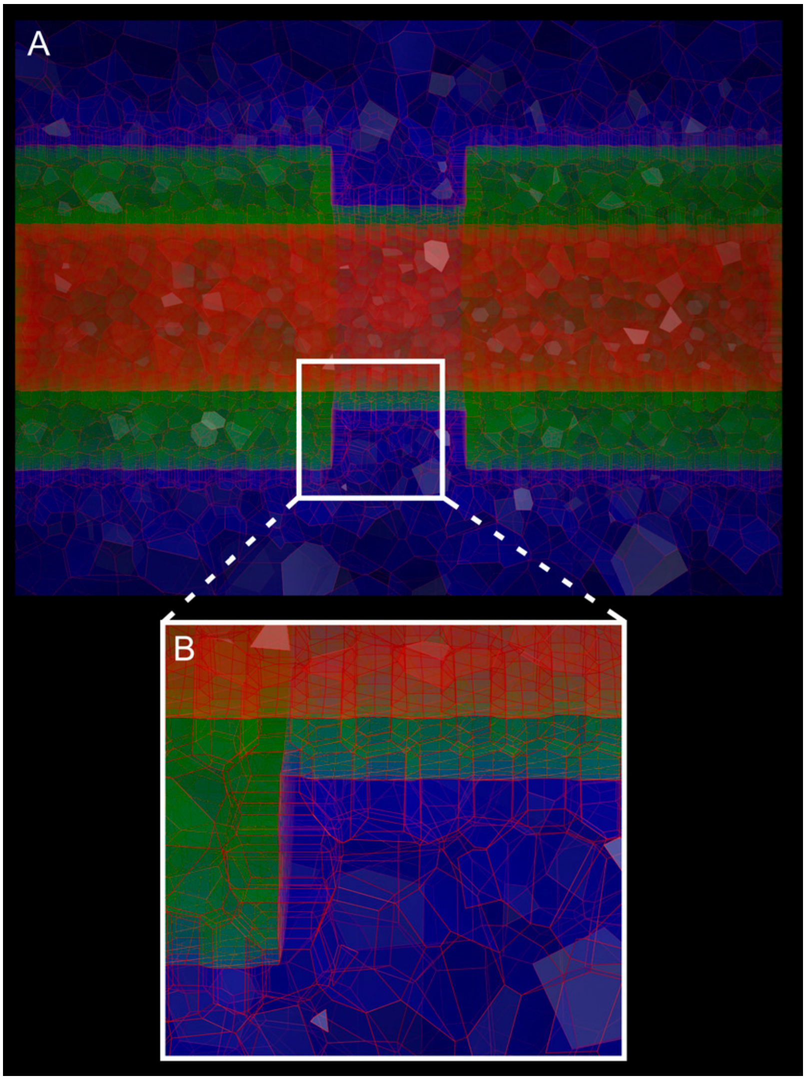

FIGURE 3 Voronoi mesh for 3D finite volume method. (*A*) Cross section through 4 μm length of axon; extracellular space is shown in blue, membrane is shown in green, and intracellular space is shown in red. The volume has been decomposed into Delaunay tetrahedra (not shown) and Voronoi volume elements whose boundaries are outlined as red wire-frame polyhedra. The region highlighted by the white frame is shown magnified in *B*.

Electrodiffusion method

One of the advantages of the electrodiffusion method is the ability to simulate the large-scale diffusion of ions in three dimensions. In doing so, consequences of ion accumulation and depletion around geometrically irregular structures can be observed without modeling the diffusion of each individual ion explicitly as is done in single particle methods. Furthermore, the electric field can be computed in space and time due to the corresponding motion of the ions. This section describes the implementation of the Poisson-Nernst-Planck equations using a Delaunay-Voronoi volume mesh. The algorithm consists of three major sections. The first section describes the initialization of the routine where initial extracellular and intracellular concentrations and voltages are uniformly distributed in space. The second section outlines the equilibration of the ions without a stimulus. Since the initial concentrations are only rough estimates, Eqs. 10–19 need to be solved, using a small time step of 100 ps, to find the actual concentrations and voltages that satisfy the Poisson-Nernst-Planck equations. The third section describes the generation of the membrane action potential. An outline of the method follows:

Initialization

Step 1. Read in Delaunay-Voronoi mesh file containing $\varepsilon, \Delta S, \Delta R$, and $\Delta\Omega$.

Step 2. Initialize concentrations. Concentrations of ions are those typical of the squid giant axon and are given in Table 1. The intracellular concentration of anions was slightly increased (by 0.02 mM) so that the inside of the nodal complex is slightly more negative (−65 mV) inside relative to the outside to model a small potassium leak. The concentrations are uniformly distributed.

Step 3. Initialize potential. Inside is uniformly −65 mV and the outside is uniformly 0 mV.

Step 4. Define channel locations in the nodal segment. Initialize channel gating parameters.

Equilibration

Step 1. Using Eq. 5, calculate charge density in each Voronoi volume element.

Step 2. Solve Poisson

Eq. 15:

a. Calculate A_{ii} and A_{ij} using Eqs. 17 and 18.

b. Solve Eq. 16 using the Gauss-Seidel algorithm (11), and iterate until

$$\frac{|V_i^k - V_i^{k-1}|}{|V_i^{k-1}|} \leq 0.001 \; k = 1, N_{\text{iterations}}.$$

Step 3. Calculate Eqs. 11 and 12 to obtain voltage and concentration gradients across each face.

TABLE 1 Electrodiffusion parameters

D_K	1.96e–5 cm^2/s	Diffusion constant for K$^+$	Hille (6)
D_{Na}	1.33e–5 cm^2/s	Diffusion constant for Na$^+$	Hille (6)
D_{Cl}	2.03e–5 cm^2/s	Diffusion constant for Cl$^-$	Hille (6)
D_A	2.00e–5 cm^2/s	Diffusion constant for A$^-$	Average value from Hille (6)
$[K^+]_{in}(0)$	155 mM	Initial inner potassium ion concentration [K$^+$]	Hille (6)
$[Na^+]_{in}(0)$	12 mM	Initial inner sodium ion concentration [Na$^+$]	Hille (6)
$[Cl^-]_{in}(0)$	4.2 mM	Initial inner chloride ion concentration [Cl$^-$]	Hille (6)
$[A^-]_{in}(0)$	162.802 mM	Initial inner organic ion concentration [A$^-$]	Neutrality from Hille (6) + offset
$[K]_{out}(0)$	4 mM	Initial outer potassium ion concentration [K$^+$]	Hille (6)
$[Na]_{out}(0)$	145 mM	Initial outer sodium ion concentration [Na$^+$]	Hille (6)
$[Cl]_{out}(0)$	123 mM	Initial outer chloride ion concentration [Cl$^-$]	Hille (6)
$[A^-]_{out}(0)$	26 mM	Initial outer organic ion concentration [A$^-$]	Neutrality from Hille (6)
T	6.3°C	Temperature	Default temperature for squid kinetics Hines and Carnevale (1)
$C_{m,node}$	2 μF/cm^2	Nodal membrane capacitance	Frankenhaeuser and Huxley (14)
$C_{m,axon}$	0.5 μF/cm^2	Axonal membrane capacitance	
ε_o	8.854e–8 μF/cm	Permitivity of vacuum	
R	8.31454 C.V/mol.K	Gas constant	
F	9.6485e4 C/mol	Faraday's constant	
d_{node}	0.1 μm	Nodal membrane thickness	Scaled value from Sosinsky et al. (10)
d_{myelin}	0.406 μm	Myelin membrane thickness	Sosinsky et al. (10)
$Diam_{axon}$	0.868	Axon diameter	Sosinsky et al. (10)
R_{bath}	2 μm	Bath radius	
l_{node}	0.7 μm	Nodal length	Sosinsky et al. (10)
l_{myelin}	1.65 μm	Myelin length	Sosinsky et al. (10)
G_{Na}	0.12 S/cm^2	Sodium channel conductance	Hodgkin and Huxley (12)
G_K	0.036 S/cm^2	Potassium channel conductance	Hodgkin and Huxley (12)
G_{leak}	0.0003 S/cm^2	Potassium leak channel conductance	Hodgkin and Huxley (12)
V_{rest}	−68.58 mV	Resting membrane potential	
$Stim_{dur}$	0.5 ms	Stimulus duration	
$Stim_{amp}$	10 pA	Stimulus amplitude	

Step 4. Calculate flux across each face using Eq. 10.

Step 5. Solve Eq. 13 for the species concentration using a fixed time step of 100 ps. A small time step is chosen to ensure numerical stability since the initial intracellular voltage gradients are large.

Step 6. Repeat steps 1–5 until concentrations reach a steady state. The criterion is

$$\frac{|V_i^t - V_i^{t-1}|}{|V_i^{t-1}|} \le 0.001 \;\; t = 1, N_{\mathrm{time}}.$$

Action potential generation

Step 1. Using Eq. 5, calculate charge density in each Voronoi volume element.

Step 2. Solve Poisson Eq. 15:

a. Calculate A_{ii} and A_{ij} using Eqs. 17 and 18.

b. Solve Eq. 16 using the Gauss-Seidel algorithm (11), and interate until

$$\frac{|V_i^k - V_i^{k-1}|}{|V_i^{k-1}|} \le 0.001 \;\; k = 1, N_{\mathrm{iterations}}.$$

Step 3. Calculate Eqs. 11 and 12 to obtain voltage and concentration gradients across each face.

Step 4. Calculate the flux across each face using Eq. 10.

Step 5. Find time step, dt. If $|V_i^t - V_i^{t-1}|/|V_i^{t-1}| \le 0.001$, increase time step from 100 ps to a maximum of 1.5 μs. If $|V_i^t - V_i^{t-1}|/|V_i^{t-1}| > 0.001$, decrease time step to a minimum of 100 ps.

Step 6. Solve Eq. 13 for the species concentration.

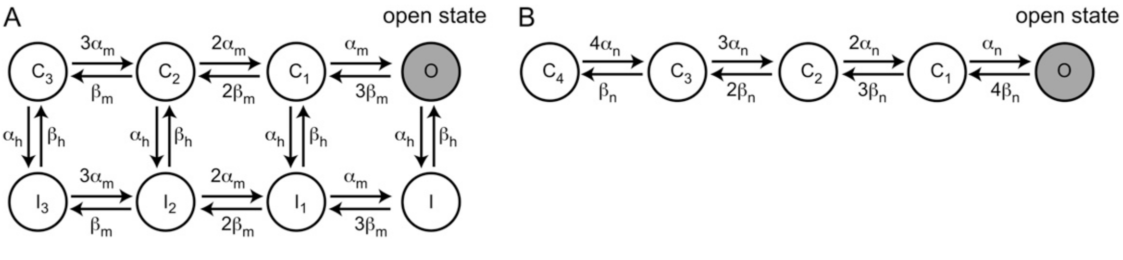

FIGURE 4 Stochastic kinetic models of (*A*) sodium (6) and (*B*) potassium channels (13). Closed states (*C*), open states (*O*) and inactivated states (*I*) are shown with rate constants indicated on the transitions between them.

TABLE 2 Cable model parameters

$[K^+]_{in}(0)$	155 mM	Initial inner potassium ion concentration $[K^+]$	Hille (6)
$[Na^+]_{in}(0)$	12 mM	Initial inner sodium ion concentration $[Na^+]$	Hille (6)
$[K]_{out}(0)$	4 mM	Initial outer potassium ion concentration $[K^+]$	Hille (6)
$[Na]_{out}(0)$	145 mM	Initial outer sodium ion concentration $[Na^+]$	Hille (6)
T	6.3°C	Temperature	Default temperature for squid kinetics Hines and Carnevale (1)
$C_{m,node}$	2 μF/cm^2	Nodal membrane capacitance	Frankenhaeuser and Huxley (14)
$C_{m,axon}$	0.5 μF/cm^2	Axonal membrane capacitance	
dt	1e – 5 s	Time step	
d_{node}	N/A	Nodal membrane thickness	
d_{myelin}	N/A	Myelin membrane thickness	
l_{node}	0.7 μm	Nodal length	Sosinsky et al. (10)
l_{myelin}	1.65 μm	Myelin length	Sosinsky et al. (10)
$Diam_{axon}$	0.868	Axon diameter	Sosinsky et al. (10)
G_{Na}	0.12 S/cm^2	Sodium channel conductance	Hodgkin and Huxley (12)
G_K	0.036 S/cm^2	Potassium channel conductance	Hodgkin and Huxley (12)
G_{leak}	0.0003 S/cm^2	Potassium leak channel conductance	Hodgkin and Huxley (12)
V_{rest}	−68 mV	Resting membrane potential	
$Stim_{dur}$	0.5 ms	Stimulus duration	
$Stim_{amp}$	10 pA	Stimulus amplitude	

Step 7. If time is <0.5 ms, inject current into the center of the nodal complex with an intracellular microelectrode, using a square pulse of Na^+ at 10 pA for 0.5 ms.

Step 8. Calculate ΔV across membrane at channel sites.

Step 9. Call Markovian channel routine shown in Fig. 4.

Step 10. If channel is in a permissible state for ion flow, calculate reversal potentials for K^+ and Na^+, and add charge to the Voronoi elements representing the channels. The charge for Na^+ is defined as

$$q_{Na} = -g_{Na}(\Delta V - E_{Na}) \times dt, \tag{29}$$

where g_{Na} is the individual Na^+ channel conductance given by

$$g_{Na} = G_{Na}/N_{Na^+\,channels}, \text{ and the charge for } K^+ \text{ is}$$
$$q_K = -g_K(\Delta V - E_K) \times dt - g_{leak}(\Delta V + 54.3) \times dt, \tag{30}$$

where g_K is the individual K^+ channel conductance given by

$$g_k = G_K/N_{K^+\,channels}, \text{ and } g_{leak} \text{ is the individual leak conductance given by}$$
$$g_{leak} = G_{leak}/N_{K^+\,channels}.$$

Step 11. Calculate new concentrations of channel voxels given by

$$c_k = c_k + \frac{q_k}{z_k F \Delta\Omega}. \tag{31}$$

Step 12. Repeat steps 1–11 until an end time of 10 ms.

RESULTS

Application of the electrodiffusion solver to a model node of Ranvier

After equilibrating the nodal system according to the method outlined above, the resulting voltage profile was found and is depicted in Fig. 6. The voltage outside of the cell is uniformly very close to 0 V, the myelin segments show a gradient from 0 mV to −68 mV. After equilibration, the ion channels were enabled and a membrane action potential was generated. The depolarizing stimulus caused the sodium channels to activate obeying the Markovian kinetic scheme shown in Fig. 4. Clusters of ion channels, 102 clusters of Na^+ channels and 30 clusters of K^+ channel, randomly placed at the node in discrete locations, accommodated 3060 Na^+ channels and 1080 K^+ channels in most simulations. This corresponds to a density of 1603 μm^{-2} and 840 μm^{-2}, respectively. These matched estimates obtained via experimental methods (15,16). In some simulations, the number of channels clustered at the node was increased to 30,600 Na^+ and 10,800 K^+ channels to show a reduction in stochasticity with greater numbers of channels. The total conductance summed over all channels was kept the same in all simulations in which channel numbers changed and matched the cable model conductance of 0.12 S per cm^2 for the sodium channels and 0.036 S per cm^2 for the potassium channels. The random distribution of channel clusters at the node is shown in Fig. 12.

Fig. 7 shows the computed membrane action potentials using various channel cluster sizes compared to the cable model. The simulation took 7 days to run 10 ms on a 2.2 GHz AMD Opteron 248 processor. The stochasticity can be observed for the smaller clusters, but as the cluster size increased, better agreement with the cable model was obtained. The broadening that is observed using a lower density of channels is not predicted in the cable model, demonstrating that the channels are influenced by their own local electric fields. The disagreement arises because the cable model uses continuous conductances. The noise was especially apparent in the repolarization phase because the number of K^+ channels was a third the number of Na^+ channels. We also obtained open channel probabilities for the largest cluster size and cable model. Fig. 8 *A* shows the Na^+ open channel probability and Fig.8 *B* shows the K^+ open channel probability. The results matched well with the cable model; however, there was also more noise in the closing repolarization phase. Fig. 9, *A* and *B*, show the spatial average inside and

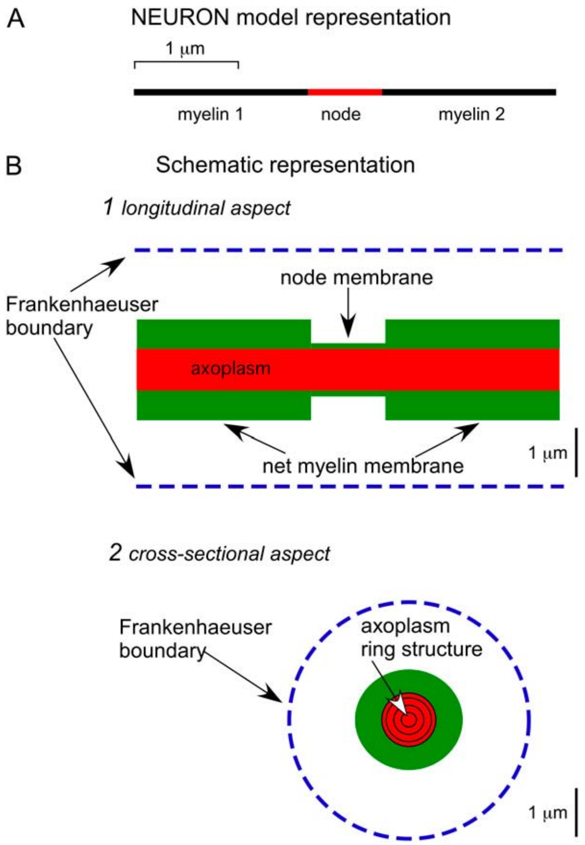

FIGURE 5 Cable model representation. (*A*) The single node of Ranvier model as displayed by the NEURON simulator (1,2). (*B*) Effective schematic representation of the node model indicating the Frankenhaeuser, or extracellular, boundaries (*dotted lines*), myelinated segments (swollen membrane), and the internal concentric ring, or cylinder, structure used to simulate axoplasmic diffusion of ions.

outside concentrations of Na^+ compared to the cable model, and Fig. 10, *A* and *B*, show the spatial average concentrations of K^+.

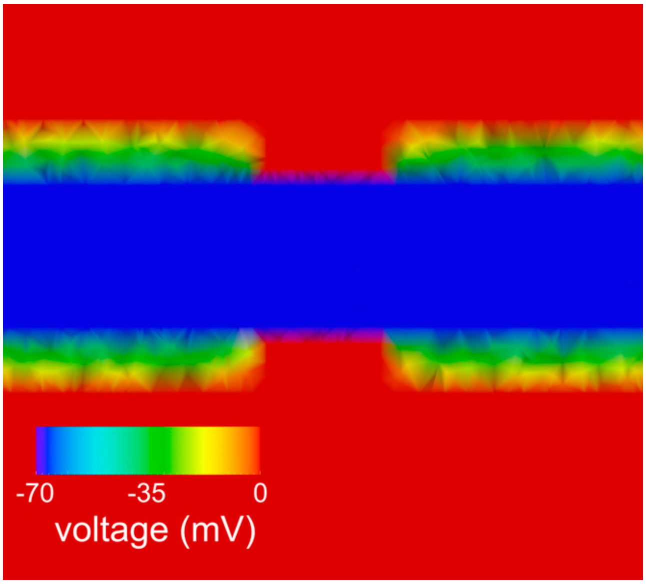

FIGURE 6 Resting membrane potential. Color bar represents millivolts.

Although average inside and outside concentrations should match with the cable model, the model does not show the precise spatial distribution of ions within the nodal region where the channels are located. Fig. 11 compares concentrations and voltages from the electrodiffusion simulation for several time steps along the action potential. Notice that at the start, the Na^+ ions, especially in the nodal region, were slightly repelled from the membrane on the inside of the cell, since the inside of the cell is more negative relative to the outside. The coarseness of the Delaunay mesh exaggerates the apparent spatial extent of this boundary layer, which is actually only ~5 nm thick. Conversely, there was a slight accumulation of Na^+ along the outside of the membrane edge. Potassium shows the same relative pattern. At 0.4 ms, there was an increase in sodium by 0.15 mM in the center of the cell where Na^+ current was injected, and there was a depletion of K^+ in the same region due to repulsion from the incoming Na^+ stimulating current. On the opposite side of the membrane, there was a slight depletion of sodium and an accumulation of potassium. The third row shows the Na^+ and K^+ distributions during peak depolarization at 0.6 ms. The inside of the cell gradually increased in Na^+ concentration as Na^+ entered through the voltage-gated Na^+ channels, and the outside of the cell along the membrane decreased in Na^+ concentration as Na^+ diffused through channels. In contrast, the K^+ concentration decreased along the inside of the membrane as K^+ exited through the K^+ channels into the extracellular space. Not surprisingly, there was an accumulation of K^+ in the extracellular nodal region. During repolarization, shown in the fourth row at 2 ms, the Na^+ concentration

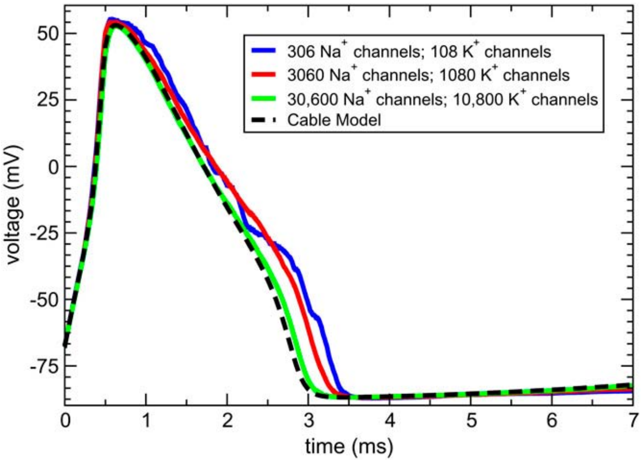

FIGURE 7 Comparison between membrane action potentials computed using the cable model (*dashed line*) and those computed by the electrodiffusion simulator evoked by injection of a square current pulse (10 pA, 0.5 ms) at the center of the node segment. Data show variable Na^+ and K^+ channel densities: 306 Na^+/108 K^+ (*blue*), 3060 Na^+/1080 K^+ (*red*), and 30,600 Na^+/10,800 K^+ (*green*). Simulations using higher densities of channels more closely resemble the cable model output.

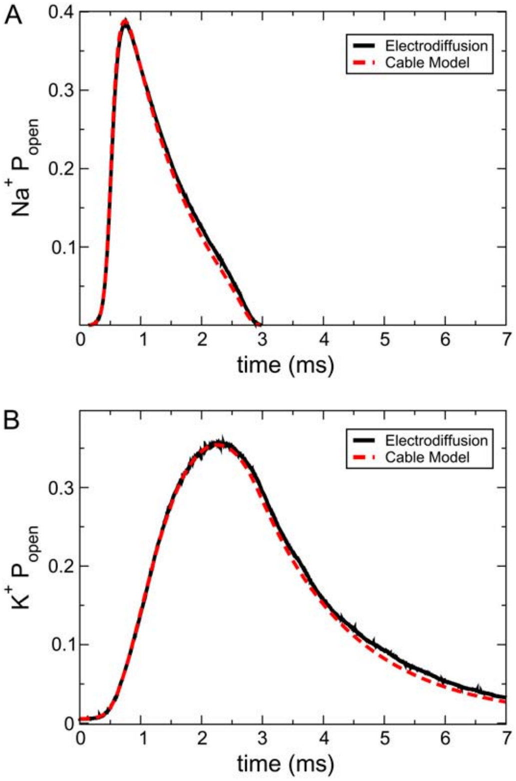

FIGURE 8 Comparison between open channel probabilities for (*A*) Na^+ and (*B*) K^+, computed by the cable model (*dashed line*) and electrodiffusion (30,600 Na^+/10,800 K^+).

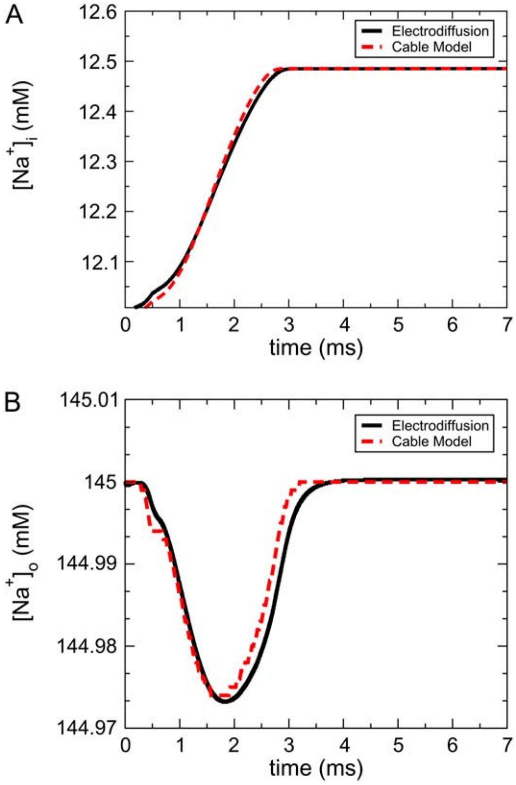

FIGURE 9 Comparison between Na^+ concentrations for (*A*) internal and (*B*) external, computed by the cable model (*dashed line*) and electrodiffusion (30,600 Na^+/10,800 K^+).

intracellularly increased to a peak value of 12.6 mM in the nodal region, and depleted by 0.1 mM on the outside edge of the node. In a cross section of extracellular space, with the axon and myelin made invisible, at this same point in time (2 ms), the depletion of Na^+ is shown in Fig. 12 *A*, whereas the accumulation of K^+ is shown in Fig. 12 *B*. At the same time, K^+ further depleted from the center of the cell to a concentration of 154.6 mM, while accumulating on the outside of the membrane by 0.04 mM. Fig. 12, *A* and *B*, also illustrates the local concentration gradients that form around channel clusters, giving rise to the local fields that affect channel gating and action potential broadening shown in Fig. 7. Finally, the fifth row of Fig. 11, *A* and *B*, shows the state of the cell at 3.4 ms during hyperpolarization, where Na^+ and K^+ ions was starting to distribute more evenly inside and outside of the cell.

DISCUSSION

With the sudden increase of three-dimensional structures from electron microscopic tomography and ever increasing computing power comes the opportunity to combine simulations with morphologically realistic depictions of cells and organelles. The node of Ranvier represents an interesting case study for further development of in silico simulation environments because of the large ionic fluxes that occur during the action potential, the complexity of the various membrane compartments from both the axon and glial cells, and the precise localizations of specific ion channel isoforms, each with its own kinetic parameters. Here, we present the initial development of a simplified node model of electrodiffusion that serves as a foundation for adding in more complex compartments and components.

The node of Ranvier complex is an intricate organization of axonal and glial membranes, small aqueous compartments, and ion fluxes. During the steepest parts of the action potential, where the currents are the greatest, there was a noticeable accumulation and depletion of ions around the node of Ranvier. Although the concentration changes may be more pronounced in this model due to the abrupt termination of the myelin at the edge of the node, which differs from a more gradual realistic cellular structure, the model provides insight into how structural irregularities and voltage gradients influence the behavior of ions. The cylindrical geometry of the node was chosen so that a comparison to a cable model could be made to validate the electrodiffusion method. As a result, details of a helical myelin structure were intentionally neglected. Extracellular details, such as a surrounding astrocyte or Schwann cell microvilli (of central nervous system or peripheral nervous system nodes, respectively), were also ne-

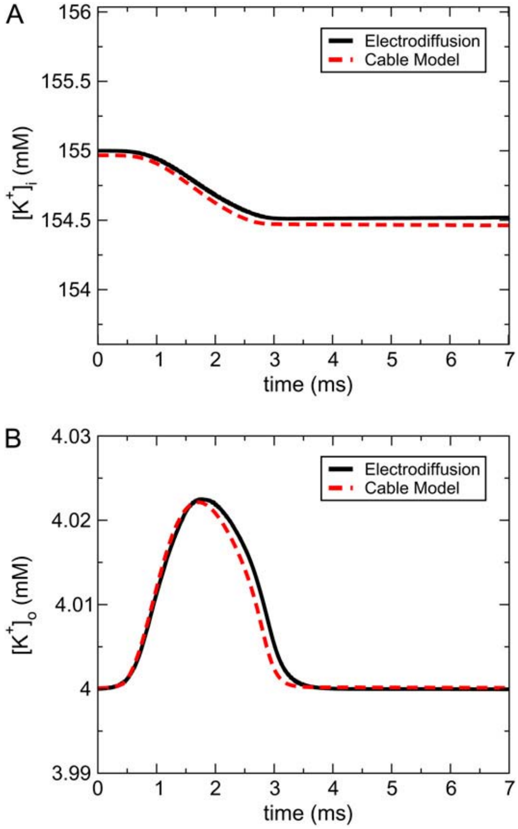

FIGURE 10 Comparison between K^+ concentrations for (*A*) internal and (*B*) external, computed by the cable model (*dashed line*) and electrodiffusion (30,600 Na^+/10,800 K^+).

glected in this model. The surrounding glial processes may provide a diffusion barrier, restricting the space surrounding the node, and may cause a more dramatic effect in the distribution of the electric field, as well as the concentrations of ions, especially in the case of central nervous system nodes where the spaces appear most restricted.

Potassium channel clusters were concentrated at the node in our model, instead of being concentrated in regions adjacent to the node, in the juxtaparanodal regions as occurs in situ. When channels were distributed along the myelin, in the region adjacent to the node, the effects of accumulation and depletion were virtually absent, even though the individual channel conductances were the same (data not shown). This may lend some insight into how action potentials become amplified at nodes. Furthermore, the geometric irregularities found in myelinated axons may allow diffusional eddies to form near the nodes, where ions tend to accumulate solely due to the spatial properties of the axon. This effect is noticeable in Figs. 11 and 12; however, there is some discretization error associated with using a volume mesh with corners.

A future study will incorporate more realistic channel locations and kinetics for a mammalian node of Ranvier, where the myelin will be represented by a helical structure found in the 3D tomographic structure (10). Currently, this is intractable until the algorithms presented here are parallelized. Accurate extracellular spatial detail will be included, so that more can be understood about the role of the channels as well as how the electric field changes. The electrodiffusion method allows channels to be distributed in different ways, and gating parameters can be altered to match various experimental scenarios. Electrodiffusion is significant since the voltages surrounding individual channels determine how they gate, and each ion channel individually responds to its local electrochemical gradient. When fewer channels were used, a broadening of the action potential was observed, which indicated a higher concentration of intracellular potassium during repolarization. The broadening, due to the response of the voltage-gated channels to their local environment, will be useful in understanding stochastic channel closures and other biophysical effects around the small volumes at nodes of Ranvier, as well as other biological systems. Hopefully, it will be possible in the not too distant future to determine the veracity of these computationally derived modeling results experimentally via advances in high resolution biophotonic imaging methods (17–19).

Although the current model has been applied to the node of Ranvier, there are other biophysical processes such as the generation/transmission of cardiac impulses and synaptic transmission where the algorithms developed in this article can also be applied. This methodology will prove useful in cases where the effects of localized fluxes of ions or differential ionic concentrations may be significantly larger because they are confined in smaller structures.

CONCLUSIONS

The methods in this article describe an algorithm to simulate electrodiffusion in three dimensions. The simulator predicts the distribution of ions in and around a model node of Ranvier due to diffusion and electric field effects at physiologically relevant voltages and ion concentrations. Ion channel opening causes electrochemical gradients, significant in small volumes, and the electrochemical gradients alter the diffusion rate of ions, impacting the time course of signaling. The electrodiffusion results are in agreement with the cable model for large cluster sizes; however, for smaller densities of channels, there was a broadening of the action potential. The broadening, corresponding to a longer repolarization phase, may lead to slower transmission where frequency-dependent conduction is an issue. Increasing the cluster sizes causes a greater depletion in the vicinity of the channels, thereby repolarizing the membrane at a more substantial rate. The three-dimensional model is essential when looking at specific gradients in nodal complex regions of small volumes. Ions need to diffuse in three dimensions to accurately predict accumulation and depletion effects. The study presented here lays the foundation for more extensive work and a more detailed analysis that includes more complex and geometrically accurate models from reconstructions, as well as to incorporate specific details of ion motion around ion channels. Fur-

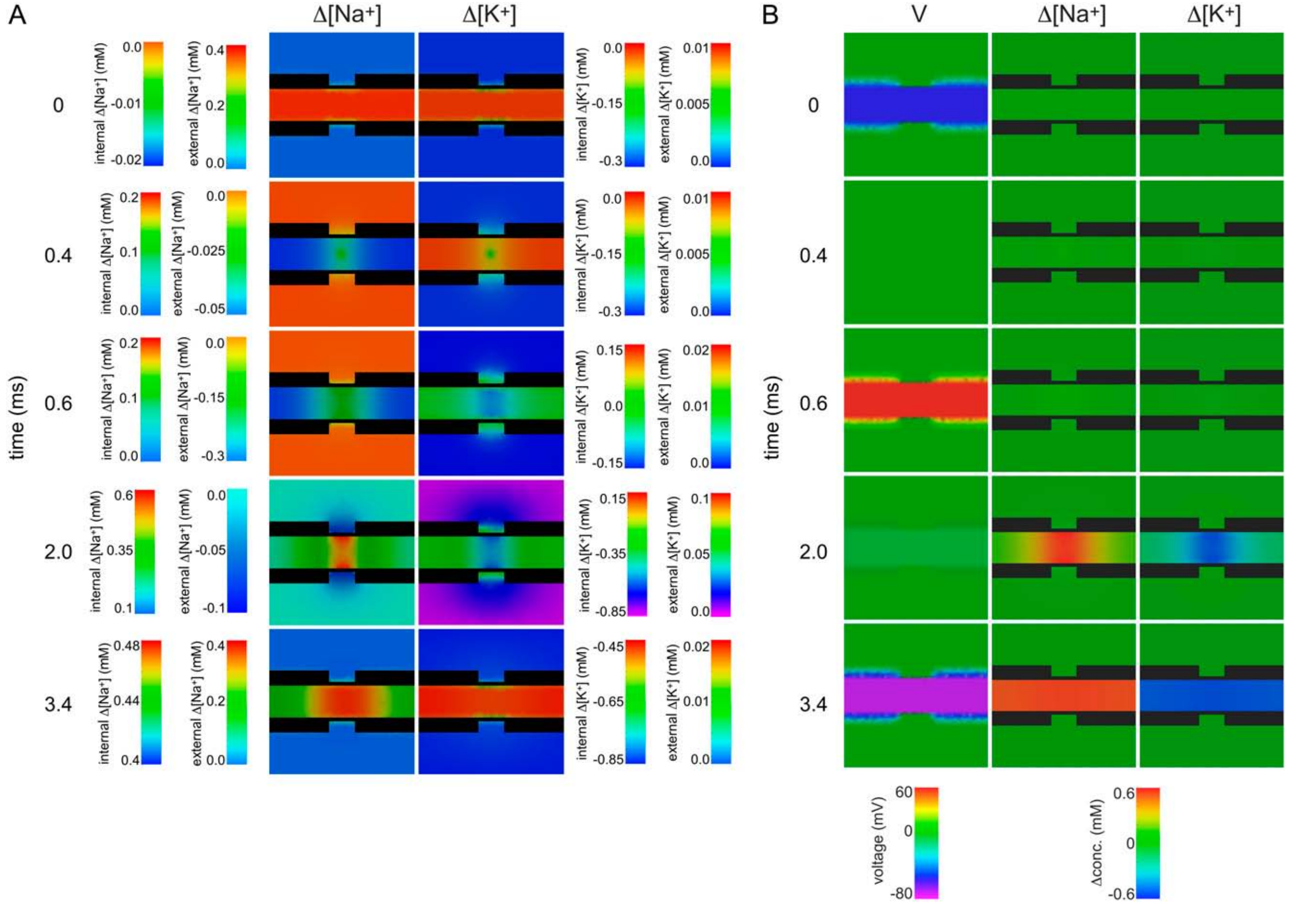

FIGURE 11 Diagram of 2D cross section through node of Ranvier showing voltage and difference in concentration from nominal resting values (given in Table 1) along time course of action potential curve at several time points: 0 ms (at rest), 0.4 ms (depolarization), 0.6 ms (peak), 2.0 ms (repolarization), and 3.4 ms (hyperpolarization). Concentration difference values are in millimolars, and voltage values are in millivolts. (*A*) Concentration differences displayed with color bars individually adjusted to reveal full range of differences. (*B*) Voltage and concentration differences displayed with common color bars to allow direct comparison of values across time points.

thermore, since the computed action potentials agree with the cable model, the model under some scenarios can be used in future studies to generate a stimulus, and multiple action potentials can be modeled. In investigating conduction failure or hyperexcitability, the electrodiffusion simulator can be used to monitor the responses of ions to sudden changes in conductivity, providing more insight into the consequences of action potential broadening.

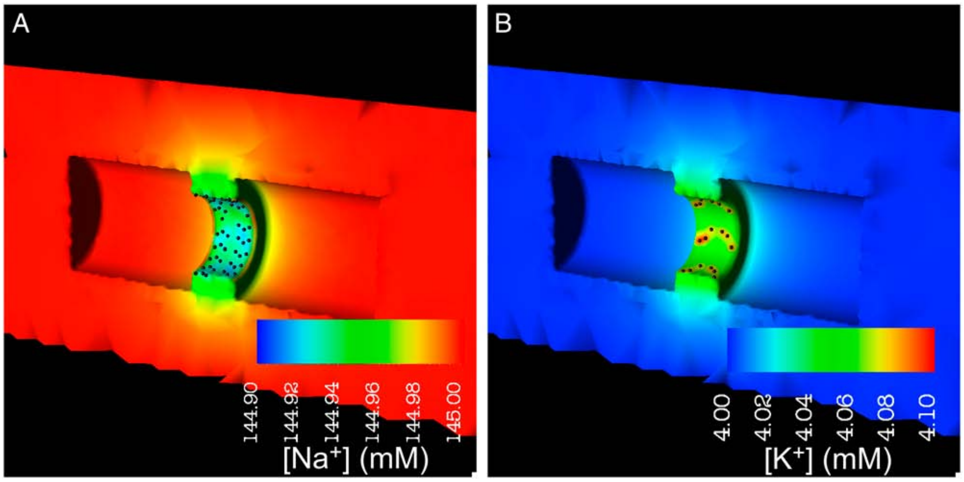

FIGURE 12 Cross section through extracellular space with the axon and myelin made invisible for (*A*) Na^+ concentration and (*B*) K^+ concentration at 2.0 ms. Locations of channel clusters are indicated by black dots.

The authors thank Harold Trease, Andrew McCammon, Michael Holst, Rick Lawrence, Don Gaver, Ricardo Cortez, and Lisa Fauci for helpful discussions and Jane Kim for her efforts in the node of Ranvier volume segmentation.

This work was supported in part by the Howard Hughes Medical Institute (C.L.L., T.J.S.), National Institutes of Health (NIH) GM068630 (T.J.S., T.M.B.), Center for Theoretical Biological Physics (National Science Foundation PHY0225630 (T.J.S., T.M.B.)), NIH (RR004050, NS046068, and NS014718 (M.H.E.)), National Science Foundation MCB0543934 (G.E.S.) and GM065937 (G.E.S.), and the Center for Computational Science at Tulane University (NIH 1 P20 EB001432-01).

REFERENCES

1. Hines, M. L., and N. T. Carnevale. 1997. The NEURON simulation environment. *Neural Comput.* 9:1179–1209.
2. Hines, M. L., and N. T. Carnevale. 2001. NEURON: a tool for neuroscientists. *Neuroscientist.* 7:123–135.
3. Bhalla, U. S. 1998. The Network within: Signalling Pathways. *In* The Book of GENESIS: Exploring Realistic Neural Models with the GEneral NEural SImulation System, 2nd ed. J. M. Bower and D. Beeman, editors. Springer-Verlag, New York.
4. Rall, W. 1969. Time constants and electrotonic length constants of membrane cylinders and neurons. *Biophys. J.* 9:1483–1508.
5. Rall, W. 1977. Core conductor theory and cable properties of neurons. *Handb. Physiol.* 1:39–97.
6. Hille, B. 2001. Ion Channels of Excitable Membranes. Sinauer Associates, Sunderland, MA.
7. Qian, N., and T. J. Sejnowski. 1989. An electro-diffusion model for computing membrane potentials and ionic concentrations in branching dendrites, spines, and axons. *Biol. Cybern.* 62:1–15.
8. van Egeraat, J. M., and J. P. Wikswo. 1993. A model for axonal propagation incorporating both radial and axial ionic transport. *Biophys. J.* 64:1287–1298.
9. Jack, J. J. B., D. Noble, and R. W. Tsien. 1975. Electric Current Flow in Excitable Cells. Oxford University Press, Oxford.
10. Sosinsky, G. E., T. J. Deerinck, R. Greco, C. H. Buitenhuys, T. M. Bartol, and M. H. Ellisman. 2005. Development of a model for microphysiological simulations. *Neuroinformatics.* 3:133–162.
11. Press, W. H., S. A. Teukolsky, W. T. Vetterling, and B. P. Flannery. 1992. Numerical Recipes in Fortran 77: The Art of Scientific Computing. Cambridge University Press, New York.
12. Hodgkin, A. L., and A. F. Huxley. 1952. A quantitative description of membrane current and its application to conduction and excitation in nerve. *J. Physiol.* 117:500–544.
13. Destexhe, A., Z. F. Mainen, and T. J. Sejnowski. 1994. Synthesis of models for excitable membranes, synaptic transmission and neuromodulation using a common kinetic formalism. *J. Comput. Neurosci.* 1:195–230.
14. Frankenhaeuser, B., and A. F. Huxley. 1964. The action potential in the myelinated nerve fibre of *Xenopus laevis*, as computed on the basis of voltage clamp data. *J. Physiol.* 171:302–315.
15. Ellisman, M. H. 1979. Molecular specialization of the axon membrane at nodes of Ranvier are not dependent upon myelination. *J. Neurocytol.* 8:719–735.
16. Ellisman, M. H., and S. R. Levinson. 1982. Immunocytochemical localization of sodium channel distributions in the excitable membranes of *Electrophorus electricus*. *Proc. Natl. Acad. Sci. USA.* 79: 6707–6711.
17. Gustafsson, M. G. L., D. A. Agard, and J. W. Sedat. 1999. I5M: 3D widefield light microscopy with better than 100 nm axial resolution. *J. Microsc.* 195:10–16.
18. Gugel, H., J. Bewersdorf, S. Jakobs, J. Engelhardt, R. Storz, and S. W. Hell. 2004. Cooperative 4Pi excitation and detection yields sevenfold sharper optical sections in live cell microscopy. *Biophys. J.* 87:4146–4152.
19. Baker, B. J., H. Lee, V. A. Pieribone, L. B. Cohen, E. Y. Isacoff, T. Knopfel, and E. K. Kosmidis. 2007. Three fluorescent protein voltage sensors exhibit low plasma membrane expression in mammalian cells. *J. Neurosci. Methods.* 161:32–38.